Quantifying octahedral rotations in strained perovskite oxide films

S. J. May,[1,2,*] J.-W. Kim,[3] J. M. Rondinelli,[4] E. Karapetrova,[3] N. A. Spaldin,[4] A. Bhattacharya,[1,5] and P. J. Ryan[3]
[1]*Materials Science Division, Argonne National Laboratory, Argonne, Illinois 60439, USA*
[2]*Department of Materials Science and Engineering, Drexel University, Philadelphia, Pennsylvania 19104, USA*
[3]*Advanced Photon Source, Argonne National Laboratory, Argonne, Illinois 60439, USA*
[4]*Materials Department, University of California, Santa Barbara, California 93106, USA*
[5]*Center for Nanoscale Materials, Argonne National Laboratory, Argonne, Illinois 60439, USA*
(Received 25 June 2010; published 20 July 2010)

We have measured the oxygen positions in $LaNiO_3$ films to elucidate the coupling between epitaxial strain and oxygen octahedral rotations. The oxygen positions are determined by comparing the measured and calculated intensities of half-order Bragg peaks, arising from the octahedral rotations. Combining *ab initio* density-functional calculations with these experimental results, we show how strain systematically modifies both bond angles and lengths in this functional perovskite oxide.

DOI: 10.1103/PhysRevB.82.014110 PACS number(s): 61.05.cp, 68.55.−a

I. INTRODUCTION

Strain engineering is an appealing route to controlling electronic,[1] ferroic,[2–4] and structural properties in complex oxide heterostructures.[5,6] The sensitivity to strain arises from the strong electron-, spin-, and orbital-lattice coupling inherent to ABO_3 perovskite oxides.[7–9] Previous work has demonstrated how strain-based manipulation of bond lengths via octahedral distortions can be used to enhance ferroelectricity.[10,11] A less explored, yet perhaps equally productive route for enhanced functionality is the manipulation of octahedral rotations in epitaxial films.[12–14] As these rotations are intimately linked to the electronic structure, strain-based control of *B*-O-*B bond angles* is a promising strategy for tailoring magnetism, metal-insulator transitions, and superconductivity. However, the current understanding of strain bond-angle relationships is limited, in part, due to the experimental challenge of measuring oxygen positions in thin films. Transmission electron microscopy has been used to identify rotational patterns,[15] visualize oxygen atoms, and measure their displacements[16] but quantification of oxygen positions remains challenging. Both extended x-ray absorption fine structure and multiple diffraction rod analysis techniques have provided insight into octahedral rotations and distortions in perovskite films,[17–21] however the complexity associated with the data analysis has limited their extensive use in perovskite film studies. The development of an additional experimental technique that is both quantitative and relatively straightforward to perform would make the measurement of octahedral rotations more accessible and lead to a greater understanding of atomic structure in strained films.

Octahedral rotations reduce the *B*-O-*B* bond angles from the ideal 180° by offsetting the oxygen atoms from the face-centered positions. These rotations can occur about the pseudocubic (a) [1 0 0], (b) [0 1 0], and/or (c) [0 0 1] directions;[22–24] the corresponding rotation angles are referred to as α, β, and γ, respectively, and are depicted in Fig. 2(a). Glazer notation is used to describe the phase of the rotations along each axis. A superscript, appended to each axis, indicates whether neighboring octahedra rotate in-phase ($^+$), out-of-phase ($^-$), or if rotations are absent (^{0}).[22] The octahedral rotations effectively double the pseudocubic unit cell, producing a distinctive set of half-order Bragg peaks depending on the rotation pattern.[25]

While half-order peaks have been employed previously to identify crystallographic space groups of perovskite films,[26] in this work we demonstrate how these Bragg peaks can be used to quantify the octahedral rotations in strained perovskite oxide films. The oxygen positions are obtained by comparing the intensities of half-order Bragg peaks with the calculated structure factor of the oxygen octahedra. Combining the diffraction results with density-functional theory (DFT) calculations, we examine the evolution of the rotation angles with strain for a model functional oxide. We show how epitaxial strain systematically alters bond angles and lengths, demonstrating that *both* octahedral rotations and distortions play a crucial role in strain accommodation. The relative simplicity of the experimental approach, requiring only high-flux x-ray diffraction (XRD) and the calculation of structure factors, makes this a promising strategy for determining the full atomic structure of a broad range of strained perovskite films.

We chose to study $LaNiO_3$ (LNO) as an example because it exhibits octahedral rotations along each axis. Bulk LNO has an $a^-a^-a^-$ rotation pattern ($\alpha=\beta=\gamma=5.2°$) with $R\bar{3}c$ symmetry and a pseudocubic lattice parameter of 3.838 Å.[27] This results in uniform Ni-O-Ni bond angles of 165.2° and Ni-O bond lengths of 1.935 Å. The isotropic nature of bulk LNO is ideally suited to explore how strain alters bond lengths and angles in an anisotropic manner. Additionally, LNO has garnered interest due to its novel properties such as electric-field control of conductivity,[28] correlated Fermi-liquid behavior,[29] and predictions of superconductivity.[30]

II. DIFFRACTION MEASUREMENTS

Epitaxial LNO films were deposited on $SrTiO_3$ (STO) ($a=3.905$ Å) and $LaAlO_3$ (LAO) ($a=3.795$ Å) substrates by molecular-beam epitaxy[31] in order to probe how both tensile (1.7% on STO) and compressive (−1.1% on LAO) strain modifies the film's atomic structure. The films grown on STO and LAO are 173-Å-thick and 95-Å-thick, respectively,

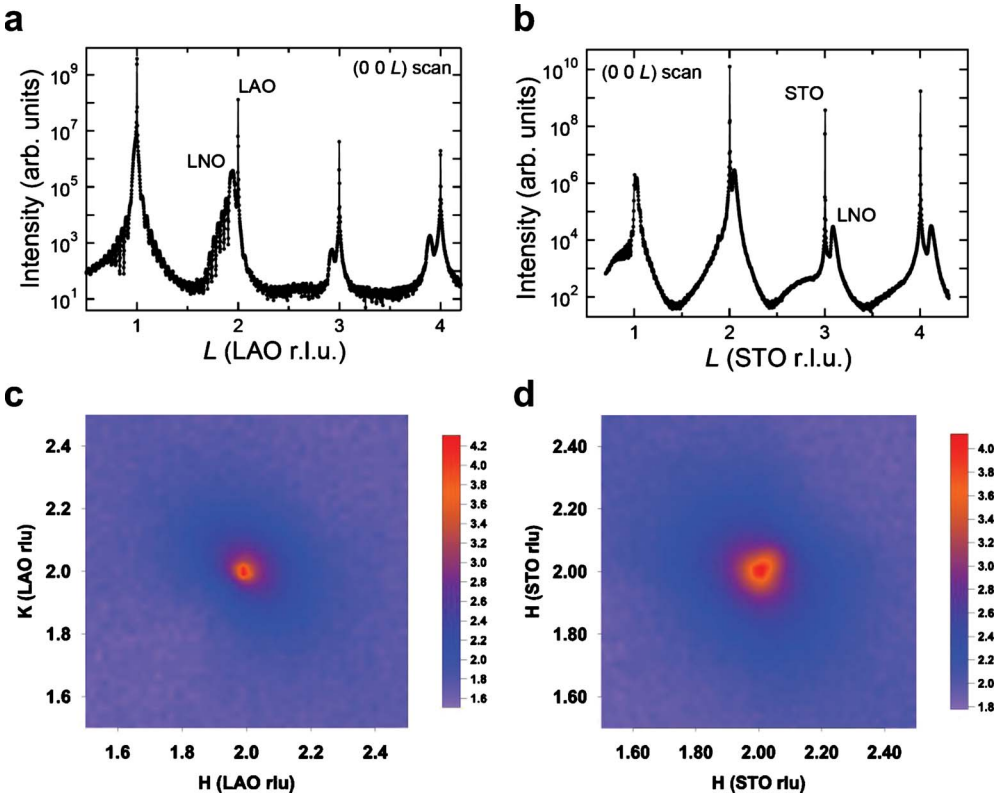

FIG. 1. (Color online) Extended (00*L*) scans of LNO grown on (a) LAO and (b) STO. Reciprocal space maps obtained near the (2 2 1.946) condition (LNO/LAO) and (2 2 2.05) condition (LNO/STO) confirm that both films are strained [(c) and (d)]; the intensity is plotted on a log scale. In all cases, the reciprocal-lattice units are set to those of the substrate.

and coherently strained with *c*-axis parameters of 3.807 and 3.895 Å as confirmed by reciprocal space maps and (00*L*) scans. These results are shown in Fig. 1. All diffraction measurements were performed at the Advanced Photon Source on Sectors 33-BM and 6-ID at room temperature.

In addition to exploring how strain modifies the octahedral distortions, growing on the two substrates, STO and LAO, enables us to investigate how the substrates' structural properties interact with the octahedral rotations of the LNO films through heteroepitaxy. For example, STO is cubic at room temperature and lacks octahedral rotations whereas LAO is rhombohedral with the $a^-a^-a^-$ rotation pattern. Thus, by measuring the structural distortions in the LNO/STO films, we can determine whether octahedral rotations are suppressed when growing on a cubic substrate. Similar analysis of the distortions in the LNO films on LAO enables us to determine if the rotational pattern present in the substrate couples to that found in the film. Additionally, we investigated LNO on cubic $(La_{0.18}Sr_{0.82})(Al_{0.59}Ta_{0.41})O_3$ (LSAT) substrates. However, intense, broad half-order peaks presumably due to antiphase boundaries in the LSAT obscured the half-order peaks in the film.

The rotation pattern of the LNO films is identified by observing the presence and absence of specific half-order Bragg peaks. We find half-order peaks in the films grown on both substrates [Figs. 2(b) and 2(c)], which confirms that heteroepitaxial growth on a cubic substrate does not suppress octahedral rotations. Both films exhibit half-order peaks when the following conditions are met: (1) h, k, and l are equal to $n/2$, where n is an odd integer and (2) $h=k\neq l$, $k=l\neq h$, and $h=l\neq k$. Peaks are not observed where $h=k=l$, such as $(\frac{1}{2}\frac{1}{2}\frac{1}{2})$, or where one of the indices is equal to an integer, such as $(\frac{1}{2}1\frac{3}{2})$. This reciprocal lattice indicates the presence of an $a^-a^-c^-$ tilt pattern within both films,[25] with $\alpha=\beta$ due to the biaxial strain state of the films ($a=b$).

The intensities of the half-order peaks are compared to calculated peak intensities in order to quantify the octahedral rotation angles. The peak height is used as the measure of peak intensity, as scans through various half-order peaks along the h and l directions indicate that the peak widths are equal, independent of their location on the reciprocal lattice. The calculated peak intensities are determined from Eq. (1),

$$I = I_0 \frac{1}{\sin(\eta)} \frac{1}{\sin(2\Theta)} \left(\sum_{j=1}^{4} D_j |F_{hkl}|^2 \right), \tag{1}$$

where I_0 is the incident photon flux, $1/\sin(\eta)$ is a correction for the beam footprint, $1/\sin(2\Theta)$ is the Lorentz polarization correction, F_{hkl} is the structure factor for the oxygen atoms, and D_j is the relative volume fraction of structural domains discussed below. The incident photon angle is η while the scattering angle is Θ. The structure factor for each Bragg peak is obtained from

$$F_{hkl} = f_{O^{2-}} \sum_{n=1}^{24} \exp[2\pi i(hu_n + kv_n + lw_n)], \tag{2}$$

where the position of the nth oxygen atom within the unit cell is given by (u,v,w), and $f_{O^{2-}}$ is the O^{2-} form factor.[32]

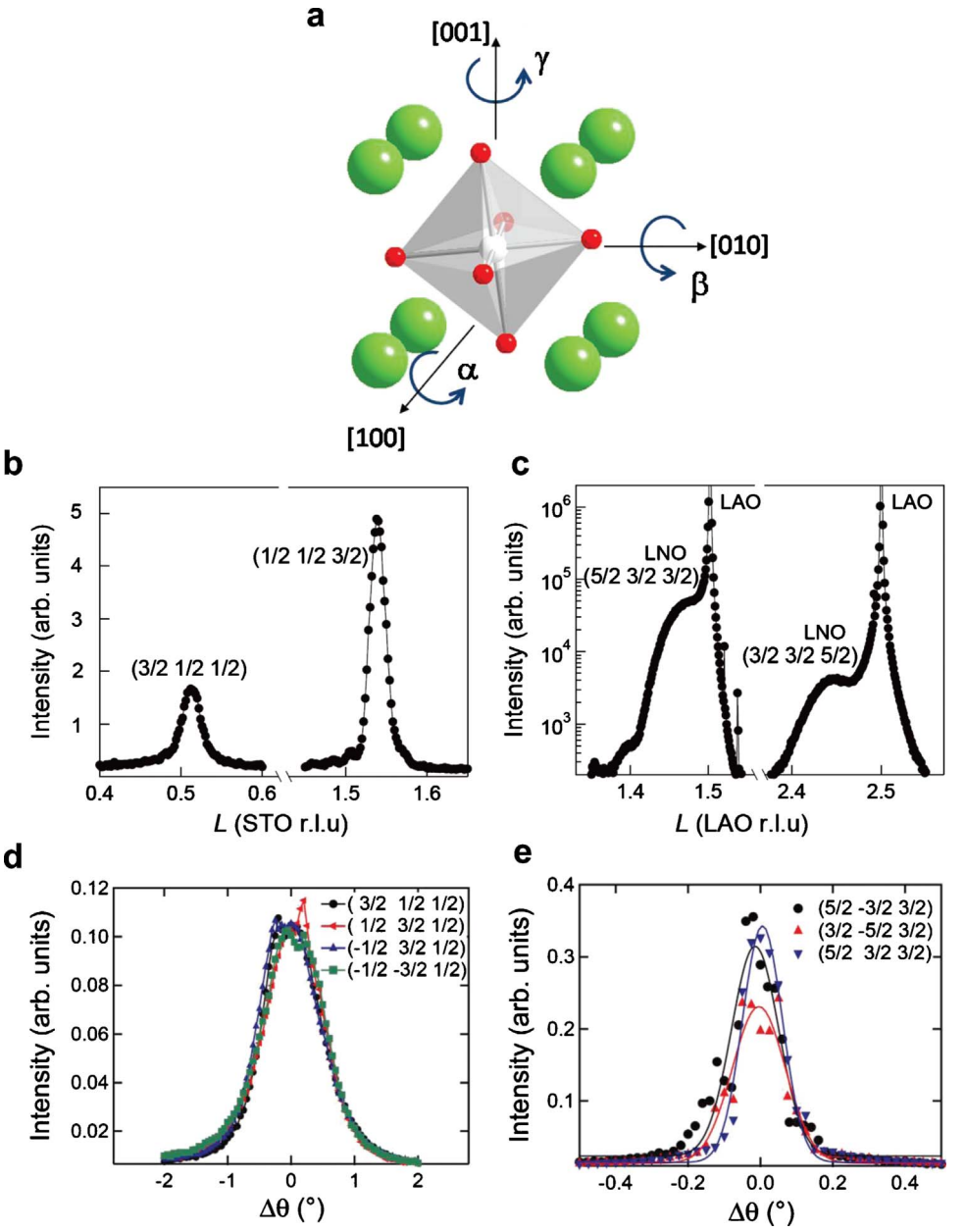

FIG. 2. (Color online) The rotation axes in (a) perovskites. Half-order peaks arising from the octahedral rotations in LNO on (b) STO and (c) LAO. In LNO/STO, the $h=k$ peaks are more intense than those with $h\neq k$, as $\alpha>\gamma$. The opposite intensity pattern is observed for LNO/LAO, as $\alpha<\gamma$. Intense half-order peaks from rotations in the LAO are also present. The contribution from the LAO peaks to the film peaks is $<10\%$. Rocking curves measured through symmetrically equivalent half-order peaks confirming the equal domain populations in (d) LNO/STO and the unequal populations in (e) LNO/LAO.

The La and Ni atoms are assumed to reside on the ideal corner and body-centered positions, respectively, and thus we do not consider a rhombohedral distortion of the La positions. Antiparallel displacements of the La or Ni atoms were also considered, however such displacements would give rise to a $(\frac{1}{2}\frac{1}{2}\frac{1}{2})$ peak, which is not produced by octahedral rotations. Experimentally, we confirmed that $h=k=l$ half-order peaks are not present in the films. Therefore, only the contributions from oxygen atoms are considered in our analysis. We account for the octahedral rotations by doubling the unit cell in each direction, giving rise to a nonprimitive unit cell consisting of 24 oxygen positions. The oxygen positions are displaced from the face-centered positions by the appropriate rotation angle.

To calculate the intensity of a given peak, the relative volume of the structural domains (D_j) is needed. These domains determine whether the octahedron nearest to the chosen origin rotates clockwise or counterclockwise about each axis. Within this rotation pattern, there are four domains that give rise to different structure factors: one where α, β, and γ are all positive, and three where two of the angles are positive and the third is negative. The domain volume fractions are obtained from a set of symmetrically equivalent half-order peaks with fixed l, for instance, $(\pm\frac{1}{2}\pm\frac{1}{2}\frac{3}{2})$, the relative

a

Peak	Meas. I/I_0	Calc. I/I_0
$(\bar{1}\,1\,\frac{5}{2})$	1.0	1.0
$(1\,1\,\frac{5}{2})$	1.2	1.0
$(\bar{1}\,1\,\frac{7}{2})$	0.46	0.49
$(\bar{1}\,1\,\frac{9}{2})$	0.04	0.08
$(1\,1\,\frac{3}{2})$	5.8	6.0
$(1\,\bar{3}\,\frac{3}{2})$	1.3	1.3

b

Peak	Meas. I/I_0	Calc. I/I_0
$(\frac{1}{2}\,\bar{1}\,\frac{5}{2})$	1.0	1.0
$(\frac{\bar{1}}{2}\,\bar{1}\,\frac{5}{2})$	2.4	2.2
$(\frac{1}{2}\,\bar{1}\,\frac{7}{2})$	0.56	0.60
$(\frac{\bar{1}}{2}\,\bar{1}\,\frac{7}{2})$	1.2	1.3
$(\frac{1}{2}\,\bar{1}\,\frac{9}{2})$	0.09	0.20
$(\frac{5}{2}\,\bar{3}\,\frac{3}{2})$	44.1	50.5
$(\frac{3}{2}\,\bar{5}\,\frac{3}{2})$	39.9	31.7
$(\frac{5}{2}\,\bar{3}\,\frac{3}{2})$	18.2	20.0
$(\frac{3}{2}\,\bar{5}\,\frac{3}{2})$	37.9	25.7
$(\frac{7}{2}\,\bar{3}\,\frac{3}{2})$	3.0	3.6
$(\frac{\bar{7}}{2}\,\bar{3}\,\frac{3}{2})$	0.75	0.51
$(\frac{3}{2}\,\bar{7}\,\frac{3}{2})$	0.62	0.61

FIG. 3. The measured and calculated peak intensities for (a) LNO/STO and (b) LNO/LAO.

intensities of which depend directly on the domain populations. We employ standard nonlinear regression analysis to determine the optimal values of α and γ and their respective errors.

The films grown on cubic STO and rhombohedral LAO substrates exhibit different domain populations. In the LNO/STO film, we find an equal volume fraction of the four possible domains, indicating that the four domains are energetically equivalent when LNO is grown on a cubic substrate [Fig. 2(d)]. In contrast, the LNO/LAO film shows unequal domain populations between only two domains [Fig. 2(e)], with an approximate 1:2 ratio. To explain this difference, we note that our LAO substrates contain extensive twinning, which we observed as two distinct peaks in ω scans rocked about a (0 0 l) peak. For our LAO substrate, the ratio of the two peaks is also 1:2 suggesting that the octahedral rotations and domain pattern of the substrate are transferred to the film. Since the rhombohedral distortion determines the trigonal axis about which the octahedra rotate in bulk LAO, this result demonstrates that substrates may be used to texture octahedral rotations by choosing appropriate substrate orientations. Imprinting of rotational behavior with heteroepitaxy may be an additional pathway to controlling interfacial properties in oxides.

For LNO on STO, we obtain $\alpha=\beta=7.1\pm0.2°$ and $\gamma=0.3\pm0.7°$. For LNO on LAO, we obtain $\alpha=\beta=1.7\pm0.2°$ and $\gamma=7.9\pm0.9°$. The measured and calculated peak intensities for both samples are given in Fig. 3. Knowing the rotation angles, and thus the oxygen positions, the atomic structures are obtained (Fig. 4).

a

		Experiment			Theory		
Atom	Wyckoff	x	y	z	x	y	z
La	4e	0	0.25	0.25	0	0.246	0.25
Ni	4c	0.25	0.25	0	0.25	0.25	0
O(1)	4e	0	0.810	0.25	0	0.811	0.25
O(2)	8f	0.282	0.001	0.283	0.284	0	0.284
La	4e	0	0.25	0.25	0	0.248	0.25
Ni	4c	0.25	0.25	0	0.25	0.25	0
O(1)	4e	0	0.765	0.25	0	0.771	0.25
O(2)	8f	0.257	0.034	0.292	0.258	0.040	0.299

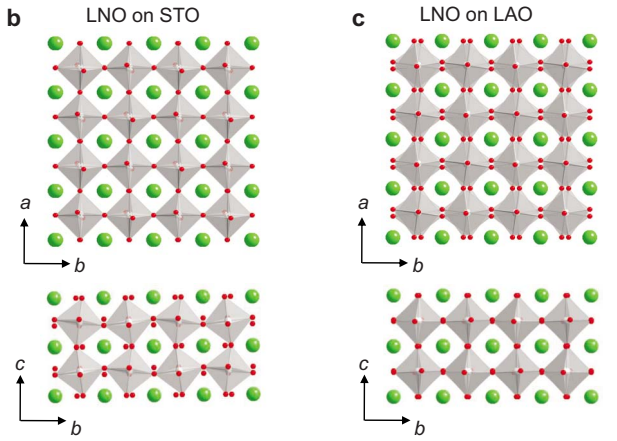

FIG. 4. (Color online) Atomic structure of LNO films as determined by diffraction (Experiment) and DFT (Theory). In (a), the top data set corresponds to LNO/STO while the bottom data set corresponds to LNO/LAO. The space group is $C2/c$ (No. 15), with $a=9.406$ Å, $b=c=5.523$ Å, and a monoclinic angle of 125.95° for LNO/STO and $a=9.460$ Å, $b=c=5.367$ Å, and a monoclinic angle of 124.57° for LNO/LAO. (b) Tensile strain reduces the γ rotation while increasing the α and β rotations. (c) Compressive strain increases the γ rotation while decreasing the α and β rotations.

As anticipated, the strain strongly modifies the in-plane (equatorial) Ni-O bond lengths ($d_{\text{Ni-O}}$) due to coherency across the heterointerface. The in-plane $d_{\text{Ni-O}}$ decreases systematically from LNO/STO (1.968 ± 0.002 Å) to bulk LNO (1.935 Å) to LNO/LAO (1.916 ± 0.005 Å) as the a- and b-axis parameters of the substrate are reduced. The measured out-of-plane (apical) $d_{\text{Ni-O}}$, however, are less sensitive to the strain; we obtain 1.933 ± 0.002 Å and 1.950 ± 0.002 Å for LNO/STO and LNO/LAO, respectively. Interestingly, we find that biaxial strain only weakly modifies the in-plane Ni-O-Ni bond angle (θ) of $165.8\pm0.5°$ and $164.0\pm2.0°$ for

TABLE I. The bond angles and lengths as determined by XRD and DFT.

	LNO/STO (XRD)	LNO/LAO (XRD)	LNO/STO (DFT)	LNO/LAO (DFT)
$d_{in\text{-}plane}$ (Å)	1.968 ± 0.002	1.916 ± 0.005	1.970	1.921
$d_{out\text{-}of\text{-}plane}$ (Å)	1.933 ± 0.002	1.949 ± 0.002	1.935	1.950
$\theta_{in\text{-}plane}$ (deg)	165.8 ± 0.5	164.0 ± 2.0	164.7	161.5
$\theta_{out\text{-}of\text{-}plane}$ (deg)	159.9 ± 0.6	175.2 ± 0.6	159.3	173.7

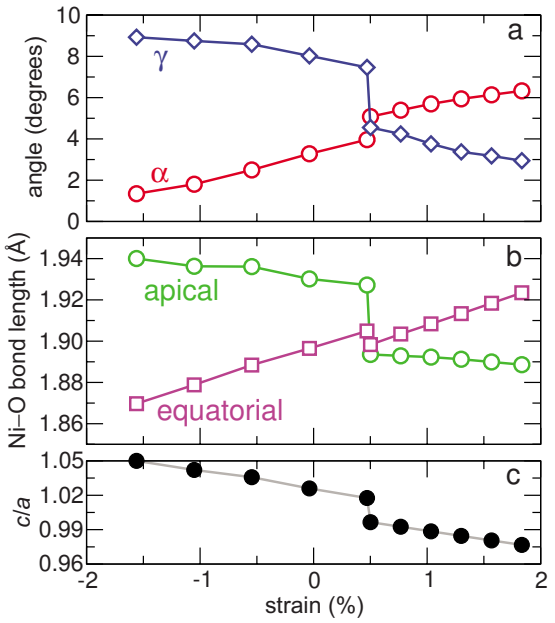

FIG. 5. (Color online) (a) The DFT calculated rotation angles, (b) Ni-O bond lengths, and (c) the c/a axial ratio as a function of strain (open symbols). A first-order transition occurs at approximately $c/a=1$.

LNO/STO and LNO/LAO, respectively. In contrast, the out-of-plane θ is highly sensitive to the substrate-induced strain; this bond angle decreases from $175.2\pm0.6°$ in LNO/LAO to $159.9\pm0.6°$ in LNO/STO. The insensitivity of the in-plane θ can be understood as both the α (or β) and γ angles contribute to the in-plane θ, and we find empirically that the average of α and γ is robust to strain. Table I summarizes the bonding data for the two samples.

III. DENSITY-FUNCTIONAL CALCULATIONS

To investigate the origin of these effects and to determine the rotational behavior for intermediate strain values, we perform DFT calculations within the local-spin density approximation (LSDA) plus Hubbard U method ($U_{\text{eff}}=U-J=3$ eV) as implemented in the Vienna *ab initio* simulation package (VASP).[33–36] We follow the Dudarev approach[34] and include an effective Hubbard term $U_{\text{eff}}=U-J$ of 3 eV to accurately treat the correlated Ni $3d$ orbitals. The core and valence electrons are treated with the projector-augmented wave method[37] with the following valence-electron configurations: $5p^6 5d^1 6s^2$ (La), $3p^6 3d^9 4s^1$ (Ni), and $2s^2 2p^4$ (O). The Brillouin-zone integrations are performed with a Gaussian smearing of 0.05 eV over a $5\times5\times5$ Monkhorst-Pack k-point mesh[38] centered at Γ, and a 450 eV plane-wave cutoff. For structural relaxations we also used a Gaussian broadening technique of 0.05 eV and relaxed the ions until the Hellmann-Feynman forces are less than 1 meV Å^{-1}. In all calculations, ferromagnetic spin order is enforced. We first optimize the internal degrees of freedom for bulk rhombohedral LNO (10-atom unit cell) at the experimental lattice parameters to confirm that we accurately describe the electronic and atomic structure. Consistent with the experimental data, our optimized structure is indeed metallic and consists of equal and alternating phase rotations of the NiO_6 octahedra about each Cartesian axis with $\alpha=\beta=\gamma=5.76°$, in good agreement with the 1.5 K structural measurement of 5.37°.[27]

The structural optimization for the two films was carried out using the experimentally determined lattice parameters. The substrates are not explicitly simulated in our calculations but the symmetry reduction imposed by enforcing equal in-plane lattice parameters on the bulk $R\bar{3}c$ structure is included by optimizing the internal degrees of freedom within a monoclinic (20-atom) unit cell (space group $C2/c$). The excellent consistency between our experimentally and theoretically obtained structures is apparent in Fig. 4(a). We note that the DFT ground state indicates an additional energy lowering distortion through small antiparallel displacements of ~0.01 Å for the La atoms along the [110] directions. Such displacements would produce weak but measurable $(\frac{1}{2}\frac{1}{2}\frac{1}{2})$ and $(\frac{3}{2}\frac{3}{2}\frac{3}{2})$ peaks, which however were not observed in the diffraction measurements, and likely persists in the DFT calculations due to the common exchange-correlation functional underestimation of the equilibrium volume.

We extend our analysis to intermediate strain states to investigate the region between the experimental values. In this section, we carry out structural relaxations about the theoretical LSDA+U equilibrium volume rather than at the experimental lattice parameters reported previously. We explore biaxial strain states by fixing the in-plane lattice constants at each strain value, and performing full structural optimizations of the internal atomic coordinates and c-axis parameter about the LSDA+U reference structure. In Fig. 5(a), we show that over the strain range investigated the

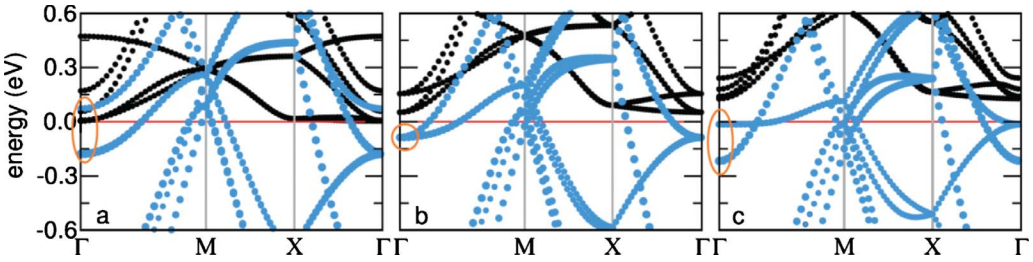

FIG. 6. (Color online) The calculated band structure of $LaNiO_3$ on (a) $LaAlO_3$, (b) bulk $LaNiO_3$, and $LaNiO_3$ on (c) $SrTiO_3$ along high-symmetry lines in the Brillouin given as $\Gamma(0,0,0)\rightarrow M(1/2,1/2,0)\rightarrow X(1/2,0,0)\rightarrow\Gamma(0,0,0)$. For each strain state, $LaNiO_3$ remains metallic. The role of strain on the electronic structure is to partially split the orbital degeneracy between the majority-spin $d_{x^2-y^2}$ and $d_{3z^2-r^2}$ orbitals (light (blue) points) as indicated at the Γ point. The Fermi level is denoted by the solid red line at 0 eV.

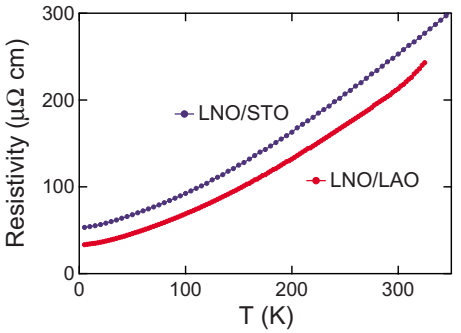

FIG. 7. (Color online) In-plane resistivity of the LNO films on LAO and STO. Both films show metallic behavior with a similar temperature dependence.

NiO_6 octahedra always rotate out-of-phase about each axis with the $a^-a^-c^-$ rotation pattern with only changes in their magnitude about each axis. In agreement with the experimental data, we find that compressive tensile strain predominately induces rotations of the NiO_6 octahedra about the c axis while tensile strain induces rotations about the in-plane axes. We attribute this effect to the epitaxial constraint that forces coherency between the film and the substrate, which contracts (elongates) the equatorial bond lengths and elongates (contracts) the apical bonds under compressive (tensile) strain [Fig. 5(b)]. The $a^-a^-c^-$ octahedral rotation pattern is able to accommodate the bond-length distortions by increasing the NiO_6 rotation about the c axis at the expense of the in-plane rotations. For the tensile case, the amount of in-plane rotation decreases accordingly to sustain the bond-length elongation in-plane. We find that there is an additional structural phase that is approximately 2 meV lower in energy for small tensile strains and shows an intriguing small charge disproportionation (CDP). The deviations in rotation angles between the two phases are negligible, and since our room temperature experiments are likely unable to access this phase, we do not discuss it further.

The transition region which captures the crossover from mainly rotations about the c axis to the in-plane axes occurs near 0.50% strain or when the axial ratio c/a approaches unity [Fig. 5(c)]. At this strain value, standard crystallographic distortion parameters that measure deviations in ideal sixfold coordination through the apical and equatorial bond lengths and the Ni-O-Ni bonds all show a sharp discontinuity and indicate almost ideal octahedra.[39] In the absence of the small CDP phase, we identify this abrupt, first-order phase transition to be *isosymmetric*[40] since the atomic structure remains monoclinic—the $C2/c$ space group is retained and the same Wyckoff positions are occupied—across the transition. The first-order phase transition about $c/a=1$ arises due to geometric constraints derived from the corner connectivity of the octahedra. Recently a strain-induced isosymmetric phase transition, with the axial ratio being the order parameter was reported in insulating thin films of the rhombohedral antiferromagnetic and ferroelectric $BiFeO_3$.[6] Since LNO and $BiFeO_3$ have distinctly different physical properties (LNO is metallic and nonpolar), we suggest this intriguing isosymmetric phase transition may be a universal feature of strained rhombohedral oxide films with the $a^-a^-c^-$ rotation pattern.

In principle, strain-induced changes to the rotation patterns can be used to tailor bandwidth-dependent properties in the thin films. In the case of the large bandwidth compound LNO, however, our DFT calculations and experiments indicate that the strain induced by the STO and LAO substrates is insufficient to produce dramatic changes in the electronic structure. The electronic band structures are shown in Fig. 6 for the two strained films on STO and LAO using the experimental nickelate structures along the high-symmetry lines in a nonprimitive $(2\times2\times1)$ unit cell of the monoclinic structure. This supercell doubles the number of bands, however, it makes the identification of the orbital contributions to the band structure more transparent. In Fig. 6(a), we show the calculated band structure for the experimentally determined nickelate film on the LAO substrate and compare it to the bulk experimental structure in Fig. 6(b) and to that on STO substrate in Fig. 6(c). For each strain state, the band structure is found to be metallic, with strain partially lifting the majority-spin e_g orbital degeneracy at the Γ point around the Fermi level. The metallic nature of the films is evident in the measured resistivity behavior, shown in Fig. 7.

IV. CONCLUSIONS

In summary, we have demonstrated a general strategy for quantifying oxygen octahedral rotations in strained complex oxide films. We have determined the atomic structure of strained $LaNiO_3$ in which the NiO_6 octahedra are distorted and rotated to accommodate strain; we suggest this mechanism is pervasive in thin-film materials with corner-shared octahedra. It is anticipated that the future application of this method will enhance fundamental studies of strain in perovskites, allow for more direct comparisons between bulk and thin film materials, and help elucidate the physical mechanisms of novel properties at oxide interfaces.

ACKNOWLEDGMENTS

Work at Argonne and use of the Advanced Photon Source was supported by the U.S. Department of Energy, Office of Basic Energy Sciences, under Contract No. DE-AC02-06CH11357. We acknowledge use of the oxide-MBE at the Center for Nanoscale Materials. We acknowledge support from NDSEG (J.M.R.) and the NSF under Grant No. DMR 0940420 (N.A.S.). This work used the SGI Altix COBALT system at the National Center for Supercomputing Applications under Grant No. TG-DMR-050002S and the CNSI Computer Facilities at UC Santa Barbara under NSF Award No. CHE-0321368.

*smay@drexel.edu

[1] T. Z. Ward, J. D. Budai, Z. Gai, J. Z. Tischler, L. Yin, and J. Shen, Nat. Phys. **5**, 885 (2009).

[2] Y. Tokura and N. Nagaosa, Science **288**, 462 (2000).

[3] D. G. Schlom, L. Q. Chen, C. B. Eom, K. M. Rabe, S. K. Streiffer, and J. M. Triscone, Annu. Rev. Mater. Res. **37**, 589 (2007).

[4] R. Ramesh and N. A. Spaldin, Nature Mater. **6**, 21 (2007).

[5] F. He, B. O. Wells, Z.-G. Ban, S.-P. Alpay, S. Grenier, S. M. Shapiro, W. Si, A. Clark, and X. X. Xi, Phys. Rev. B **70**, 235405 (2004).

[6] R. J. Zeches, M. D. Rossell, J. X. Zhang, A. J. Hatt, Q. He, C.-H. Yang, A. Kumar, C. H. Wang, A. Melville, C. Adamo, G. Sheng, Y.-H. Chu, J. F. Ihlefeld, R. Erni, C. Ederer, V. Gopalan, L. Q. Chen, D. G. Schlom, N. A. Spaldin, L. W. Martin, and R. Ramesh, Science **326**, 977 (2009).

[7] J. B. Torrance, P. Lacorre, A. I. Nazzal, E. J. Ansaldo, and C. Niedermayer, Phys. Rev. B **45**, 8209 (1992).

[8] O. Chmaissem, B. Dabrowski, S. Kolesnik, J. Mais, D. E. Brown, R. Kruk, P. Prior, B. Pyles, and J. D. Jorgensen, Phys. Rev. B **64**, 134412 (2001).

[9] T. Mizokawa, D. I. Khomskii, and G. A. Sawatzky, Phys. Rev. B **60**, 7309 (1999).

[10] K. J. Choi, M. Biegalski, Y. L. Li, A. Sharan, J. Schubert, R. Uecker, P. Reiche, Y. B. Chen, X. Q. Pan, V. Gopalan, L.-Q. Chen, D. G. Schlom, and C. B. Eom, Science **306**, 1005 (2004).

[11] J. H. Haeni, P. Irvin, W. Chang, R. Uecker, P. Reiche, Y. L. Li, S. Choudhury, W. Tian, M. E. Hawley, B. Craigo, A. K. Tagantsev, X. Q. Pan, S. K. Streiffer, L. Q. Chen, S. W. Kirchoefer, J. Levy, and D. G. Schlom, Nature (London) **430**, 758 (2004).

[12] A. T. Zayak, X. Huang, J. B. Neaton, and K. M. Rabe, Phys. Rev. B **74**, 094104 (2006).

[13] A. J. Hatt and N. A. Spaldin, arXiv:0808.3792 (unpublished).

[14] J. M. Rondinelli and N. A. Spaldin, Phys. Rev. B **81**, 085109 (2010).

[15] D. I. Woodward and I. M. Reaney, Acta Crystallogr., Sect. B: Struct. Sci. **61**, 387 (2005).

[16] C. L. Jia, S. B. Mi, M. Faley, U. Poppe, J. Schubert, and K. Urban, Phys. Rev. B **79**, 081405 (2009).

[17] A. Miniotas, A. Vailionis, E. B. Svedberg, and U. O. Karlsson, J. Appl. Phys. **89**, 2134 (2001).

[18] N. M. Souza-Neto, A. Y. Ramos, H. C. N. Tolentino, E. Favre-Nicolin, and L. Ranno, Phys. Rev. B **70**, 174451 (2004).

[19] C. K. Xie, J. I. Budnick, W. A. Hines, B. O. Wells, and J. C. Woicik, Appl. Phys. Lett. **93**, 182507 (2008).

[20] D. D. Fong, C. Cionca, Y. Yacoby, G. B. Stephenson, J. A. Eastman, P. H. Fuoss, S. K. Streiffer, C. Thompson, R. Clarke, R. Pindak, and E. A. Stern, Phys. Rev. B **71**, 144112 (2005).

[21] R. Herger, P. R. Willmott, C. M. Schlepütz, M. Björck, S. A. Pauli, D. Martoccia, B. D. Patterson, D. Kumah, R. Clarke, Y. Yacoby, and M. Döbeli, Phys. Rev. B **77**, 085401 (2008).

[22] A. M. Glazer, Acta Crystallogr., Sect. B: Struct. Crystallogr. Cryst. Chem. **28**, 3384 (1972).

[23] P. M. Woodward, Acta Crystallogr., Sect. B: Struct. Sci. **53**, 32 (1997).

[24] P. M. Woodward, Acta Crystallogr., Sect. B: Struct. Sci. **53**, 44 (1997).

[25] A. M. Glazer, Acta Crystallogr., Sect. A: Cryst. Phys., Diffr., Theor. Gen. Crystallogr. **31**, 756 (1975).

[26] F. He, B. O. Wells, and S. M. Shapiro, Phys. Rev. Lett. **94**, 176101 (2005).

[27] J. L. García-Muñoz, J. Rodríguez-Carvajal, P. Lacorre, and J. B. Torrance, Phys. Rev. B **46**, 4414 (1992).

[28] R. Scherwitzl, P. Zubko, C. Lichtensteiger, and J.-M. Triscone, Appl. Phys. Lett. **95**, 222114 (2009).

[29] R. Eguchi, A. Chainani, M. Taguchi, M. Matsunami, Y. Ishida, K. Horiba, Y. Senba, H. Ohashi, and S. Shin, Phys. Rev. B **79**, 115122 (2009).

[30] P. Hansmann, X. Yang, A. Toschi, G. Khaliullin, O. K. Andersen, and K. Held, Phys. Rev. Lett. **103**, 016401 (2009).

[31] S. J. May, T. S. Santos, and A. Bhattacharya, Phys. Rev. B **79**, 115127 (2009).

[32] E. Hovestreydt, Acta Crystallogr., Sect. A: Found. Crystallogr. **39**, 268 (1983).

[33] V. I. Anisimov, F. Aryasetiawan, and A. I. Liechtenstein, J. Phys.: Condens. Matter **9**, 767 (1997).

[34] S. L. Dudarev, G. A. Botton, S. Y. Savrasov, C. J. Humphreys, and A. P. Sutton, Phys. Rev. B **57**, 1505 (1998).

[35] G. Kresse and J. Furthmüller, Phys. Rev. B **54**, 11169 (1996).

[36] G. Kresse and D. Joubert, Phys. Rev. B **59**, 1758 (1999).

[37] P. E. Blochl, Phys. Rev. B **50**, 17953 (1994).

[38] H. J. Monkhorst and J. D. Pack, Phys. Rev. B **13**, 5188 (1976).

[39] K. Robinson, G. V. Gibbs, and P. H. Ribbe, Science **172**, 567 (1971).

[40] A. Christy, Acta Crystallogr., Sect. B: Struct. Sci. **51**, 753 (1995).